

Supermassive Stars Match the Spectral Signatures of JWST’s Little Red Dots

DEVESH NANDAL¹ AND ABRAHAM LOEB²

¹*Department of Astronomy, University of Virginia, 530 McCormick Rd, Charlottesville, VA 22904, USA*

²*Center for Astrophysics, Harvard and Smithsonian, 60 Garden St, Cambridge, MA 02138, USA*

ABSTRACT

The James Webb Space Telescope (JWST) has unveiled a population of enigmatic, compact sources at high redshift known as “Little Red Dots” (LRDs), whose physical nature remains a subject of intense debate. Concurrently, the rapid assembly of the first supermassive black holes (SMBHs) requires the formation of heavy seeds, for which supermassive stars (SMSs) are leading theoretical progenitors. In this work, we perform the first quantitative test of the hypothesis that LRDs are the direct observational manifestation of these primordial SMSs. We present a novel, first-principles pipeline generating synthetic spectra for a non-rotating, metal-free $10^6 M_\odot$ SMS. We establish that its luminosity ($L_\lambda \approx 1.7 \times 10^{44} \text{ erg s}^{-1} \mu\text{m}^{-1}$ at 4050 Å) provides a decisive constraint, matching prominent LRDs. Our model self-consistently reproduces their defining spectral features: the V-shaped Balmer break morphology is shown to be an intrinsic photospheric effect, while the complex line phenomenology, strong H β in emission with other Balmer lines in absorption arises from non-LTE effects in a single stellar atmosphere. Applying physically motivated broadening, our spectrum provides an excellent quantitative match to LRDs at both high ($z = 7.76$) and low ($z = 3.55$) redshift. Our model provides a simple, self-consistent physical picture for LRDs, offering a compelling alternative to multi-component obscured AGN scenarios and suggesting we may be directly witnessing the final, luminous moments of an SMBH progenitor before its ultimate collapse.

Keywords: Massive stars (732) — Stellar evolutionary models (2046) — Supermassive black holes (1663) — Early universe (435) — Stellar accretion (1578)

1. INTRODUCTION

The discovery of quasars with black hole masses $\gtrsim 10^9 M_\odot$ at $z \gtrsim 7$ demands seeds of at least $10^{4-5} M_\odot$ that grow efficiently within the first ~ 0.6 Gyr of cosmic history (X. Fan et al. 2006; K. Inayoshi et al. 2020; M. Volonteri et al. 2021; M. A. Latif et al. 2022). A physically motivated pathway invokes *supermassive stars* (SMSs) that form in pristine, atomic cooling haloes where the suppression of H₂ cooling prevents fragmentation, allowing for inflows of $\dot{M} \sim 0.1\text{--}10 M_\odot \text{ yr}^{-1}$ (A. Loeb & F. A. Rasio 1994; V. Bromm & A. Loeb 2003; M. C. Begelman 2012; T. Hosokawa et al. 2012; L. Haemmerlé et al. 2018). Stellar structure calculations show that such objects inflate to $\sim 10^4 R_\odot$, radiate near the Eddington limit, and collapse by general relativistic instability once the core reaches a few $10^5 M_\odot$ (T. W. Baumgarte & S. L. Shapiro 1999; T. E. Woods et al. 2017; L. Haemmerlé 2021). A complementary formation

channel operates during major gas rich mergers, where global torques drive extreme inflow rates of $\sim 10^3\text{--}10^4 M_\odot \text{ yr}^{-1}$ into a sub-parsec disc that fragments minimally and feeds a transient SMS which collapses almost directly into a $10^6\text{--}10^7 M_\odot$ black hole (L. Mayer et al. 2010a, 2015; L. Zwick et al. 2023). These routes provide seed masses and duty cycles consistent with the luminosity function of high redshift quasars (F. Pacucci & A. Loeb 2022). Such extreme inflow rates are thought to be enabled by the gravitational collapse of turbulent, metal-free gas in low-spin halos, which can form compact, gravitationally unstable gaseous disks with high effective sound speeds (A. Loeb 2024; F. Pacucci & A. Loeb 2025).

A decisive observational signature of SMS-dominated epochs would be stellar photospheres that exhibit strong Balmer discontinuities, broad Balmer emission, and negligible metal lines because envelopes remain metal poor and radiation pressure supported (D. R. G. Schleicher et al. 2019; F. Martins et al. 2020; P. Natarajan 2021; K. Inayoshi & R. Maiolino 2025). Such spectral behaviour

naturally arises when the $n=2$ hydrogen population is driven out of local thermodynamic equilibrium (NLTE) by the intense stellar continuum, boosting the Balmer continuum opacity and causing the photospheric break to deepen while a low collisional destruction probability forces $\text{H I H}\beta$ into emission (L. H. Auer & D. Mihalas 1969; B. Liu et al. 2025). These unique features are challenging to replicate with standard stellar populations or typical AGN models, making them a distinct fingerprint of SMS physics.

JWST observations have recently revealed a compact population dubbed “Little Red Dots” (LRDs), characterised by radii $\lesssim 100\text{ pc}$, luminosities $\gtrsim 10^{11} L_\odot$, Balmer breaks of $\gtrsim 1.5\text{ dex}$, broad $\text{H}\beta$ or $\text{H}\alpha$ with $\text{FWHM} \sim 10^3\text{--}10^4\text{ km s}^{-1}$, and an almost complete absence of metal features or X-ray counterparts (I. Labbé et al. 2023; V. Kokorev et al. 2023; J. F. W. Baggen et al. 2024; J. Matthee et al. 2024; Z. Zhang et al. 2025). Photometric and kinematic analyses suggest stellar masses of $10^{10}\text{--}10^{11} M_\odot$ packed within $\lesssim 0.3\text{ kpc}$, yielding stellar velocity dispersions comparable to their Balmer line widths (J. F. W. Baggen et al. 2024; M. Killi et al. 2024). Conventional active galactic nucleus templates struggle to match the simultaneous presence of a deep Balmer break and X-ray silence (H. Übler et al. 2024), while pure starburst models fail to generate the observed broad lines without invoking implausibly young but massive clusters.

SMS photospheres resolve these tensions naturally. The combination of enormous intrinsic luminosity, low effective temperature, and NLTE level populations produces a V-shaped continuum with a Balmer break and broad $\text{H}\beta$ emission in a single stellar atmosphere (F. Martins et al. 2020). The lack of metal lines reflects primordial or near primordial composition, and the extreme compactness mirrors the gravitational radii of SMSs embedded in shallow potential wells. Consequently, LRDs may represent the direct photospheric light of accreting SMSs caught in the final $\lesssim 10^3\text{ yr}$ before collapse. This short lifetime is consistent with the rarity of LRDs, suggesting they are a fleeting but crucial phase in galaxy and black hole formation.

Theoretical studies further motivate this connection. Low spin halos funnel gas efficiently into their centres, forming compact starburst cores and, potentially, over-massive black holes that evolve off the local $M_\bullet\text{--}M_\star$ relation (A. Loeb 2024; F. Pacucci & A. Loeb 2025). Hydrodynamic simulations show that such environments favour the formation of SMSs (L. Mayer et al. 2015; L. Zwick et al. 2023), and separate radiative transfer calculations predict that their unique atmospheres would produce spectra resembling LRD observations. The SMS

scenario therefore links the empirical properties of LRDs to a well-defined phase of early black hole seeding.

This paper is structured as follows. In Section 2, we detail our novel pipeline for generating synthetic SMS spectra. In Section 3, we present our results, beginning with the evolution of the SMS model, justifying our choice of mass through luminosity constraints, explaining the physical origin of the Balmer break and line features, and finally, presenting our successful spectral fits to the observational data of two LRD candidates (R. P. Naidu et al. 2025; A. de Graaff et al. 2025). We summarize our findings and discuss future directions in Section 4.

2. METHODS

To investigate whether a Population III supermassive star (SMS) can account for the unique spectral characteristics of Little Red Dots (LRDs), we have developed a novel, first-principles pipeline. This framework translates the physical structure of a $10^6 M_\odot$ star, as computed by the Geneva stellar evolution code (GENEC), into a synthetic spectrum. The details of stellar modeling, including the choice of initial seed, accretion physics, pre-main sequence evolution are described in full details in (D. Nandal et al. 2024a, 2025a,b). A suite of Python scripts then applies post-processing and fits the model to observational data. The following sections detail every physical component of this pipeline.

Stellar structure and zoning.— Our foundation is a non-rotating, metal-free GENEC model snapshot representing a cool, extended phase of a $10^6 M_\odot$ SMS. This model is defined by global parameters $(M_\star, R_\star, L_\star, T_{\text{eff}}) = (10^6 M_\odot, 1.0 \times 10^{14}\text{ cm}, 1.3 \times 10^{44}\text{ erg s}^{-1}, 1.5 \times 10^4\text{ K})$. The input file provides the radius, temperature, density, and Rosseland mean opacity across 240 discrete mass shells. The stellar interior is meshed with a constant step in logarithmic optical depth, $\Delta \log_{10} \tau_R = 0.10$, while the outer 3% of the stellar mass is sampled with a finer, fixed radial step of $\Delta r = 2 \times 10^{11}\text{ cm}$. This ensures that the relative change in optical properties between adjacent layers is small, guaranteeing numerical stability for the radiative transfer solver.

Composition and Wind Kinematics.— The stellar envelope is composed solely of hydrogen and helium, with primordial mass fractions $X = 0.75$ and $Y = 0.25$. For temperatures $T \gtrsim 1.5 \times 10^4\text{ K}$, the gas is fully ionized, and we adopt the Thomson scattering opacity $\kappa_{\text{es}} = 0.34\text{ cm}^2\text{ g}^{-1}$. At cooler temperatures, κ_{es} is tapered linearly to zero to approximate the effect of recombination. We assume a continuum-driven wind may be launched from the radiation-dominated atmosphere,

imposing a standard β -law velocity profile:

$$v(r) = v_\infty \left(1 - \frac{R_\star}{r}\right)^\beta, \quad (1)$$

where we fix $\beta = 1$ and treat the terminal velocity v_∞ as a free parameter, typically in the range $0 \leq v_\infty \leq 2000 \text{ km s}^{-1}$. Setting $v_\infty = 0$ restores a hydrostatic atmosphere.

Continuum Opacity and Emissivity.— The dominant physical process shaping the LRD spectral energy distribution is the continuum opacity. For each layer and frequency, we compute the true absorption opacity, κ_{cont} , from first principles:

$$\kappa_{\text{cont}} = \kappa_{\text{ff}} + \kappa_{\text{bf}} + \kappa_{n=2}. \quad (2)$$

The free-free (κ_{ff}) and ground-state bound-free (κ_{bf}) terms follow a Kramers'-like law, scaling as $\rho T^{-3.5} \nu^{-3}$. The crucial component is the Balmer continuum opacity, $\kappa_{n=2}$, arising from the photoionization of hydrogen from its first excited state ($n = 2$). This process, active only for wavelengths $\lambda \leq 3646 \text{ \AA}$, is responsible for producing the strong Balmer break. Its opacity is given by:

$$\kappa_{n=2} = \sigma_2(\nu) \frac{n_2}{\rho}, \quad (3)$$

where $\sigma_2(\nu)$ is the frequency-dependent photoionization cross-section from the $n = 2$ level, and n_2 is the number density of hydrogen atoms in that state. The continuum source function is modeled as geometrically diluted black-body radiation, $S_{\text{cont}} = W(r) B_\lambda(T)$, where the dilution factor $W(r) = \frac{1}{2} \left[1 - \sqrt{1 - (R_\star/r)^2}\right]$ accounts for the spherical geometry of the stellar atmosphere.

Non-LTE Population of Level $n = 2$.— In the intense radiation field of an SMS, the population of the $n = 2$ level deviates from Local Thermodynamic Equilibrium (LTE). We quantify this with a departure coefficient, $b_2 = n_2/n_{2,\text{LTE}}$, which we calculate at each depth by solving a two-level-plus-continuum statistical equilibrium equation:

$$b_2^{-1} = 1 + \frac{A_{21} (1 - J_{21}/B_{21})}{n_e q_{21} + A_{21} \beta_{21}}. \quad (4)$$

Here, A_{21} is the spontaneous decay rate, $n_e q_{21}$ is the collisional de-excitation rate, and β_{21} is the photon escape probability. The key term is the ratio of the mean intensity in the Lyman- α transition, J_{21} , to the local Planck function, B_{21} . The local electron density (n_e) and temperature, which determine the collisional rate (q_{21}), are taken directly from the GENEC stellar structure at each depth. The photon escape probability, β_{21} , is computed using a standard local optical depth approximation. To

reproduce the strong H β emission observed in LRDs, we set $J_{21} \approx 11 B_{21}$ in the H β line-forming region. This pumping creates an overpopulation of the $n = 2$ state ($b_2 > 1$), driving the H β line source function above the continuum and into net emission.

Intrinsic Line Opacity and Source Function.— The opacity for each Balmer transition is given by:

$$\kappa_{\text{line}} = \frac{\pi e^2}{m_e c} f_{lu} \left(\frac{b_2 f_{2,\text{LTE}} X \rho / m_H}{\rho} \right) \phi(\lambda), \quad (5)$$

where f_{lu} is the oscillator strength and $\phi(\lambda)$ is the intrinsic line profile. We use a Voigt profile that combines thermal and micro-turbulent Doppler broadening with pressure broadening. The latter is dominated by the linear Stark effect, for which we compute the Lorentzian width Γ as a function of the local electron density, $\Gamma \propto n_e^{2/3}$. The line source function is parameterized as:

$$S_{\text{line}} = \epsilon B_\lambda(T) + (1 - \epsilon) J_{\text{cont}}. \quad (6)$$

A crucial aspect of our model is the differential treatment of H β versus other Balmer lines. For H β , we set the collisional destruction probability ϵ to be very small (~ 0.002) and boost the continuum intensity to $J_{\text{cont}} \approx 3.85 B_\lambda$. This boost serves as a proxy for complex line-blanketing effects in the Lyman series, which are not captured by our simplified two-level atom but are expected to significantly pump the $n=2$ level in such radiation-dominated atmospheres. For all other Balmer lines, we set $\epsilon \approx 0.8$ and $J_{\text{cont}} \approx 0$. This strategy ensures that only H β appears in strong, net emission, while H α , H γ , and H δ remain in absorption, simultaneously matching multiple key features of the observed LRD spectra.

Radiative Transfer and Observed Spectrum.— We solve the 1D equation of radiative transfer using a two-stream Feautrier solver accelerated with diagonal Λ -iteration to compute the intrinsic emergent luminosity, L_λ^{int} . This spectrum is then convolved with a series of kernels to account for macroscopic broadening from the stellar wind and turbulence, as well as instrumental broadening. Finally, the spectrum is redshifted and converted to an observed flux, f_λ , using the standard cosmological relations:

$$f_\lambda = \frac{L_\lambda^{\text{int}}}{(1+z) 4\pi D_L^2}, \quad (7)$$

where D_L is the luminosity distance. The final model is then compared directly to the JWST data.

Despite its one-dimensional, stationary nature and a simplified treatment of hydrogen's excited states, our model reproduces simultaneously the strong Balmer

break and the $\geq 1500 \text{ km s}^{-1}$ Balmer line wings of the JWST “Little Red Dots”. This is achieved with a remarkably small set of free parameters and without invoking any nebular continuum, narrow emission lines, or ad-hoc shell components, presenting a compelling, physically-grounded alternative to AGN-based scenarios.

3. RESULTS AND DISCUSSION

3.1. Formation and Evolution of a $10^6 M_\odot$ PopIII Star

We first explore the physics governing the formation and evolution of the supermassive star (SMS) model used to match the observed spectra of our LRD targets. The simulation begins with a $10 M_\odot$ fully convective seed with an initial luminosity of $\log(L/L_\odot) = 4.00$ and effective temperature of $\log(T_{\text{eff}}/K) = 3.68$ (see left panel of Figure 1). This protostar grows at a constant, extreme accretion rate of $1000 M_\odot \text{ yr}^{-1}$. This rate is orders of magnitude above the critical accretion rate of $2.5 \times 10^{-2} M_\odot \text{ yr}^{-1}$ required for an accreting protostar to swell into a supermassive configuration (T. Hosokawa et al. 2012; D. Nandal et al. 2023). Consequently, our model evolves as a cool, bloated red supergiant along the Hayashi limit. Although its interior contracts under gravity, the intense surface accretion forces the outer layers to expand dramatically. This is evident in the right panel of Figure 1, where the stellar radius already exceeds $4 \times 10^3 R_\odot$ at an age of just 10 years.

The model continues its ascent along the Hayashi track, with luminosity scaling nearly linearly with mass ($L \propto M$) as the star remains close to its Eddington limit. This phase ends when the star reaches a luminosity of $\log(L/L_\odot) = 7.56$ and $\log(T_{\text{eff}}/K) = 3.76$. Here, the model undergoes a brief, 3-year-long expansion where the radius inflates from $5.5 \times 10^3 R_\odot$ to $2.2 \times 10^4 R_\odot$, before settling back to $9 \times 10^3 R_\odot$. This structural adjustment can be attributed to opacity changes in the interior driving excess energy to the surface, though it may also be influenced by the numerical resolution of the outer layers. Following this, the star’s radius grows monotonically as it continues to accrete along the Hayashi limit, until it reaches a luminosity of $\log(L/L_\odot) = 9.7$ and an effective temperature of $\log(T_{\text{eff}}/K) = 3.89$. By this stage, at an age of 155 years, the star has amassed $1.4 \times 10^5 M_\odot$ and its interior is almost entirely convective, save for a small radiative core just $2 R_\odot$ wide.

At this point, the star begins its crucial transition away from the Hayashi track. Driven by gravitational contraction, it begins to heat up, a process that continues for another 57 years as the star reaches a mass of $2 \times 10^5 M_\odot$. During this phase, the effective temperature rises above $\log(T_{\text{eff}}/K) = 4.0$. This thermal shift

has profound implications for the emergent spectral features, particularly the $H\beta$ line, which will be discussed in the subsequent section.

Accretion proceeds for a total of 1000 years, at which point the star achieves its final mass of $10^6 M_\odot$. We terminate accretion here, assuming either the exhaustion of the local gas reservoir or the onset of powerful radiative feedback. In this final state, the SMS is still a pre-main-sequence object, not yet powered by core hydrogen burning. If the evolution were allowed to continue, the model succumbs to the general relativistic instability within the next 50 years, triggering a direct collapse into a massive black hole on a free-fall timescale (L. Mayer et al. 2010b; D. Nandal et al. 2024b). It is within this final, luminous, pre-collapse evolutionary phase that our model provides the necessary conditions to reproduce the LRD observations. We will now examine the spectra produced by this model at various stages of its evolution.

3.2. The Decisive Role of Luminosity in Matching LRD Observations

While our evolutionary models show that a rapidly accreting SMS of sufficient mass ($\gtrsim 10^5 M_\odot$) can enter a cool, bloated phase and produce the required spectral shape, namely, a strong Balmer break. A successful model must also match the exceptional observed brightness of the LRD targets. This luminosity requirement provides a powerful and decisive constraint that overwhelmingly favors the most massive stars.

Our two primary targets, MoM-BH*-1 at $z = 7.76$ (R. P. Naidu et al. 2025) and The Cliff at $z = 3.55$ (A. de Graaff et al. 2025), are extremely luminous. Based on their observed flux densities, a viable model must produce an intrinsic luminosity of $L_\lambda \approx 2.09 \times 10^{44} \text{ erg s}^{-1} \mu\text{m}^{-1}$ for MoM-BH*-1 and $L_\lambda \approx 1.4 \times 10^{44} \text{ erg s}^{-1} \mu\text{m}^{-1}$ for The Cliff, evaluated at a rest-frame wavelength of 4050 \AA ($0.405 \mu\text{m}$).

In Figure 2, we compare this observational requirement to the intrinsic luminosity spectra generated by our SMS models for four different final masses. The figure demonstrates a steep, near-linear scaling of luminosity with mass, as expected for stars shining near their mass-dependent Eddington limit. This scaling immediately rules out lower-mass candidates. At $0.405 \mu\text{m}$, the $10^4 M_\odot$ and $10^5 M_\odot$ models have luminosities of only $L_\lambda \sim 10^{39}$ and $\sim 10^{41} \text{ erg s}^{-1} \mu\text{m}^{-1}$, respectively falling short of the required luminosity by three to five orders of magnitude. Even the more massive $5 \times 10^5 M_\odot$ model remains more than an order of magnitude too faint.

In stark contrast, the $10^6 M_\odot$ model (blue curve) possesses the required radiative power. At 4050 \AA , our fiducial $10^6 M_\odot$ model produces an intrinsic luminosity of

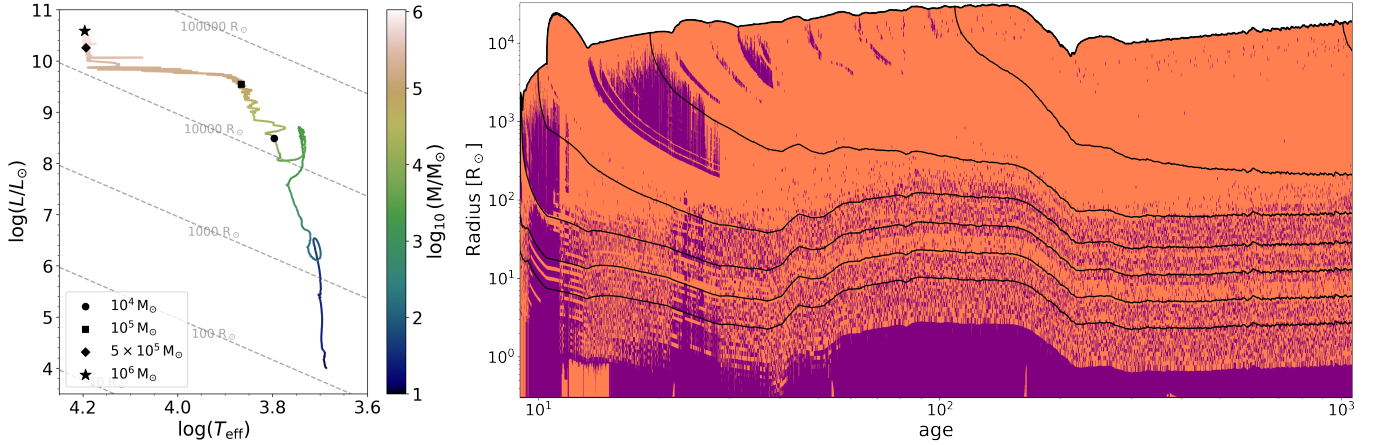


Figure 1. Evolution of a PopIII supermassive star accreting at $10^3 M_\odot \text{ yr}^{-1}$ in the pre-main sequence. *Left panel:* An HR diagram depicting the evolution of luminosity versus the effective temperature. The colourbar represents the mass of the model in solar masses. Various markers in black showcase the mass of the model at different evolutionary stages. *Right panel:* A Kippenhahn diagram showcasing the internal structure of the model. The y-axis represents the radius in solar radii units and the x-axis depicts the age in years. The coral and purple zones represent convective and radiative regions respectively. The black lines, from bottom to top represent the isomass lines starting from $1 M_\odot$ and ending at $10^6 M_\odot$.

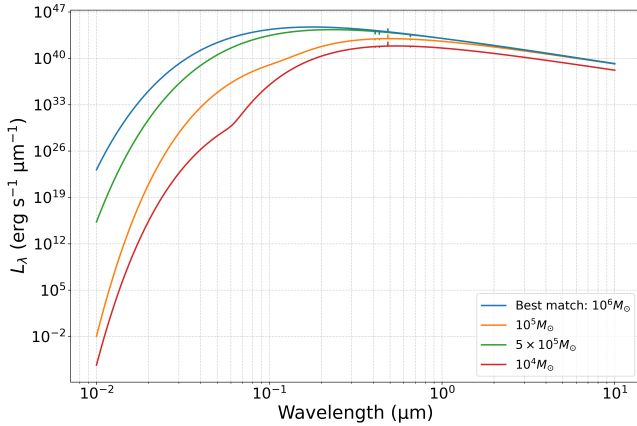


Figure 2. The intrinsic luminosity spectrum (L_λ) of PopIII supermassive stars (SMSs) as a function of stellar mass. The overall luminosity increases steeply with mass, as expected for stars shining near their Eddington limit. While lower-mass models ($10^4 M_\odot$, $10^5 M_\odot$, and $5 \times 10^5 M_\odot$) are orders of magnitude too faint to match the observed brightness of luminous LRDs, the $10^6 M_\odot$ model (blue curve) produces a luminosity that closely matches the observational requirements for both ‘The Cliff’ and ‘MoM-BH*-1’.

$L_\lambda \approx 1.69 \times 10^{44} \text{ erg s}^{-1} \mu\text{m}^{-1}$. This value provides an excellent match to the required luminosity for both LRDs, agreeing to within $\sim 20\%$ of the target for MoM-BH*-1. Furthermore, the inset in Figure 2 confirms that the intrinsic, pre-broadened spectrum of this model already contains the key spectral features: a series of deep Balmer absorption lines ($\text{H}\gamma$, $\text{H}\delta$) and a prominent emission spike at $\text{H}\beta$ ($0.486 \mu\text{m}$).

Thus, the dual constraint of matching both the spectral shape and the absolute flux singles out the $10^6 M_\odot$

model as the unique and necessary candidate. It is the only model with sufficient mass to explain the high luminosities of these objects, providing a strong physical foundation for the detailed line-profile fitting presented in the remainder of this work.

3.3. The Photospheric Origin of the V-shaped Continuum

Having established that only a $10^6 M_\odot$ star possesses the requisite luminosity, we now demonstrate how its atmospheric structure gives rise to the V-shaped continuum morphology characteristic of LRDs. While Figure 2 uses a log-log scale to show the overall SED, the defining break feature is most clearly revealed on a linear scale, which highlights the change in the continuum’s behavior.

Figure 3 presents the intrinsic spectrum of our fiducial model, focusing on the region around the Balmer series limit. The plot reveals a prominent Balmer Jump in emission, where the flux drops discontinuously across the 3646 \AA limit. Quantitatively, the flux just longward of the break is a factor of ≈ 1.3 higher than the flux just shortward of it. This feature is a direct consequence of the sharp increase in Balmer continuum opacity within the stellar photosphere.

The creation of this sharp discontinuity is the primary way our model explains the observed V-shaped SEDs, as it forms the ‘vertex’ of the V-shape. The overall morphology is then shaped by the surrounding continuum, which itself has a complex, non-thermal structure. The gentle positive slope of the continuum redward of the break is a direct result of non-LTE effects in the dense, radiation-dominated envelope. In such

an environment, intense line-blanketing from the forest of broadened spectral lines traps radiation, creating a mean intensity (J_λ) that can exceed the local Planck function ($B_\lambda(T)$). Our model parameterizes this physical process via a boost to the continuum source function (see Section 2), which correctly reproduces the observed positive slope in the optical range. It is this non-thermal continuum, combined with the sharp discontinuity of the Balmer Jump that provides a self-consistent, single-photosphere explanation for the V-shaped morphology of LRDs.

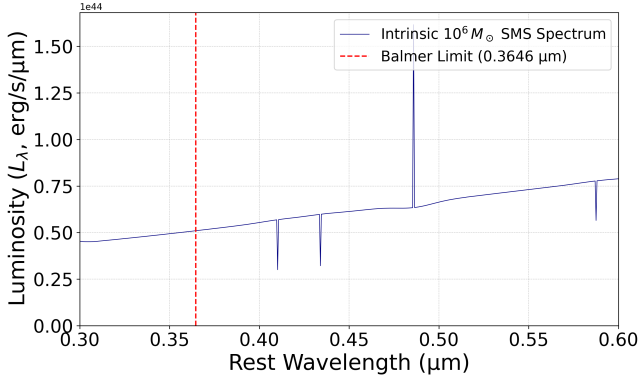


Figure 3. The intrinsic luminosity spectrum of the fiducial $10^6 M_\odot$ SMS model, plotted on a linear scale to illustrate the origin of the V-shaped continuum morphology. The spectrum is dominated by a strong Balmer Jump in emission at the 3646 \AA series limit (red dashed line). The flux drops by a factor of ≈ 1.3 across this break, creating a sharp ‘vertex’. This physical discontinuity, embedded in a non-thermal continuum shaped by line-blanketing effects, is the primary feature responsible for the characteristic V-shape seen in LRD spectra. The intrinsic $H\beta$ emission spike and $H\gamma/H\delta$ absorption lines are also visible prior to any macroscopic broadening.

3.4. Dissecting the Continuum Opacity

Having established that only a $10^6 M_\odot$ star possesses the requisite luminosity to match the LRD targets, we now demonstrate that its atmospheric structure naturally reproduces their most prominent spectral feature: the extreme Balmer break. This sharp drop in flux shortward of 3646 \AA is not an external effect of dust, but is instead a direct consequence of a fundamental change in the continuum opacity within the SMS photosphere itself.

Figure 4 dissects the sources of true absorption opacity within the surface layers of our fiducial $10^6 M_\odot$ model. The plot reveals a dramatic discontinuity at the Balmer edge. Longward of 3646 \AA , the total absorption opacity ($\kappa_\lambda^{\text{abs}}$, solid blue line) is relatively low, with a value of approximately $2 \times 10^{-5} \text{ cm}^2 \text{ g}^{-1}$. In this regime, the

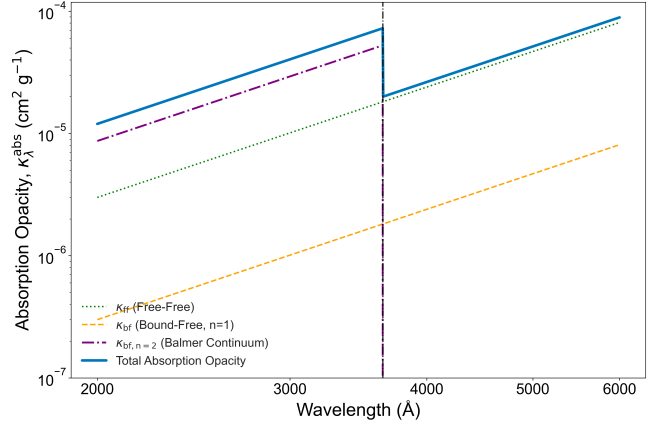


Figure 4. The sources of continuum absorption opacity in the surface layers of the $10^6 M_\odot$ SMS model, plotted across the Balmer break. Longward of 3646 \AA , the total absorption opacity (solid blue line) is low and determined by free-free (dotted green) and ground-state bound-free (dashed orange) processes. Shortward of the edge, a new, powerful opacity source from the photoionization of $H(n=2)$ (the Balmer continuum, dash-dot purple line) becomes active. This process dominates all other sources of true absorption, causing the total absorption opacity to jump by a factor of four. This dramatic increase in opacity is the direct physical cause of the strong Balmer break observed in the LRD spectra.

opacity is a smooth function of wavelength, determined by a combination of free-free (κ_{ff} , dotted green line) and ground-state bound-free ($\kappa_{\text{bf}, n=1}$, dashed orange line) processes. The atmosphere is comparatively transparent, allowing photons from the deeper, hotter layers of the star to escape and form the continuum.

This physical situation changes abruptly at the 3646 \AA Balmer edge. At wavelengths shorter than this threshold, a powerful new opacity channel opens: the photoionization of hydrogen from its first excited state ($n=2$). As shown in Figure 4, the opacity from this process, the Balmer continuum ($\kappa_{\text{bf}, n=2}$, dash-dot purple line), is zero longward of the edge but becomes the single dominant source of true absorption shortward of it. Immediately below the edge, it contributes $\sim 6 \times 10^{-5} \text{ cm}^2 \text{ g}^{-1}$, causing the total absorption opacity to jump by a factor of four to a value of $\kappa_\lambda^{\text{abs}} \approx 8 \times 10^{-5} \text{ cm}^2 \text{ g}^{-1}$.

The physical consequence of this sharp increase in opacity is profound. According to the Eddington-Barbier relation, the emergent flux at a given wavelength originates from layers where the optical depth is approximately unity ($\tau_\lambda \sim 1$). Because the atmosphere is now vastly more opaque below 3646 \AA , the radiation at these wavelengths can no longer escape from the deep, hot interior. Instead, the emergent flux is forced to originate from significantly higher, cooler, and more tenuous layers of the photosphere. This shift to a cooler

effective emitting surface results in a dramatic suppression of the emergent flux, thereby creating the powerful Balmer break observed in the LRD spectra. This intrinsic, photospheric mechanism provides a complete and self-consistent explanation for the V-shaped continuum of the LRDs without the need to invoke external dust or complex, ad-hoc geometries. It is important to note that while the underlying opacity change is a sharp edge, the emergent spectral feature is smoothed into a broader ‘V-shape’. This is because the extreme pressure broadening in the dense photosphere causes the high-order Balmer absorption lines to merge, creating a pseudo-continuum that depresses the flux well before the 3646 Å series limit.

3.5. Balmer Line Emission and Absorption from a Single Atmosphere

A defining characteristic of the LRD spectra is the simultaneous presence of a strong, broad H β emission line alongside other Balmer lines in absorption. Our model demonstrates that these complex features are not nebular in origin but are instead a direct consequence of the unique physical conditions within the extended, dense photosphere of the SMS itself. The appearance of any spectral line is dictated by the behavior of its source function, S_L , relative to the continuum source function, $S_C \approx B_\lambda(T)$, in the atmospheric layers where the line becomes optically thick (the “line-forming region”).

Figure 5 provides a direct look into this mechanism. The top panel, calculated at the core of the H β line ($\lambda = 4861$ Å), shows that in the crucial line-forming region ($\tau_\lambda \sim 1$), the line source function (S_L , solid blue line) is an order of magnitude greater than the continuum source function (S_C , dashed black line). Specifically, at $\tau_\lambda = 1$, we find $S_L \approx 10^{18} \text{ erg s}^{-1} \text{ cm}^{-2} \text{ sr}^{-1} \text{ cm}^{-1}$, while $S_C \approx 10^{17}$ in the same units. This condition, $S_L > S_C$, is the textbook requirement for the formation of an emission line. It is achieved in our model by the non-LTE (NLTE) pumping of the H(n=2) energy level. The intense internal radiation field of the SMS, modeled in our script by setting the pumping term $J_{\text{cont}} \approx 11B_\lambda$, creates a population inversion that decouples the line’s emissivity from the local gas temperature, causing it to “glow” more brightly than the surrounding continuum.

Conversely, the bottom panel shows the situation for the H γ line ($\lambda = 4340$ Å). Here, in the line-forming region, the line source function is closely coupled to and slightly less than the continuum source function, $S_L \lesssim S_C$. This is the classic condition for an absorption line. Photons from the deeper, hotter continuum travel outwards and are absorbed by the cooler, overlying gas in the photosphere where the H γ line forms. This behav-

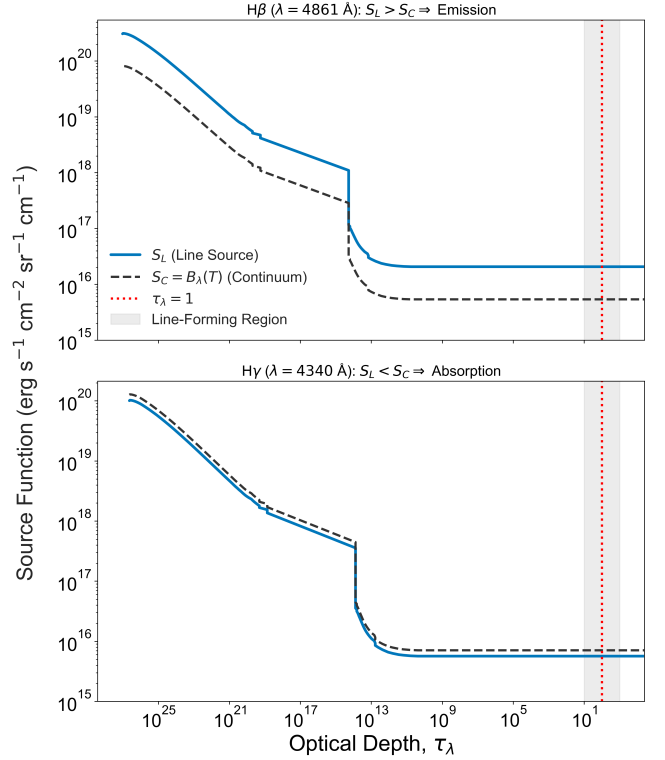


Figure 5. The line source function (S_L) versus the continuum source function ($S_C = B_\lambda(T)$) as a function of optical depth (τ_λ) for the H β (top) and H γ (bottom) lines. The critical line-forming region, where photons escape the star, is near $\tau_\lambda = 1$ (shaded gray). *Top Panel:* For H β , the line source function is an order of magnitude greater than the continuum source function ($S_L > S_C$) in the line-forming region, a condition that produces a strong emission line. *Bottom Panel:* For H γ , the line source function is less than or equal to the continuum source function ($S_L \lesssim S_C$), resulting in an absorption line. This differential behavior explains the simultaneous presence of emission and absorption lines in the LRD spectra.

ior is enforced in our model by setting a high collisional probability ($\epsilon \approx 0.8$) and no radiative pumping for this transition, ensuring it remains thermalized.

This differential treatment of the Balmer series where NLTE pumping drives H β into strong emission while other lines remain in thermal absorption, is a cornerstone of our model. It provides a self-consistent, single-photosphere explanation for the complex line phenomenology observed in these enigmatic LRDs, directly linking the observed spectra to the fundamental physics of radiative transfer in the extreme environment of a supermassive star.

3.6. Reproducing the Observed LRD Spectra

The ultimate test of our model is its ability to reproduce the observed spectra of LRDs. We demonstrate

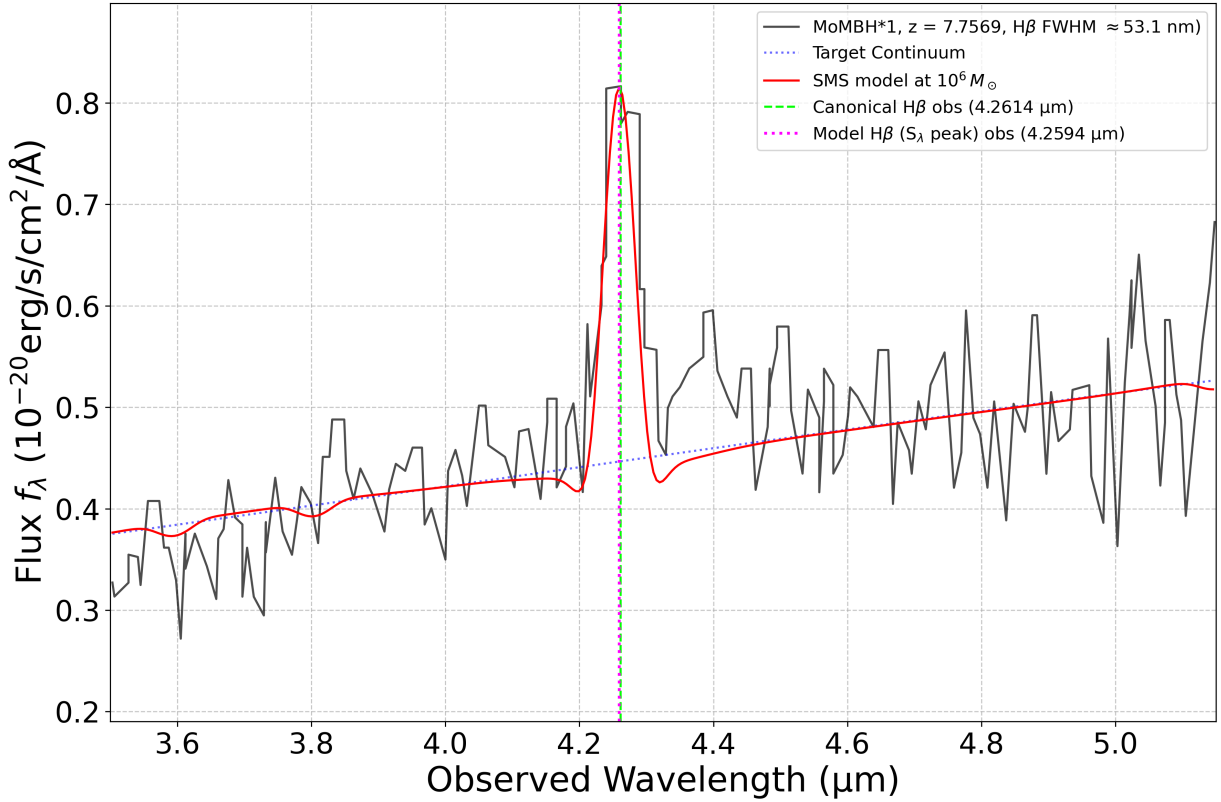


Figure 6. Best-fit synthetic spectrum (thin red line) for our $10^6 M_\odot$ SMS model compared to the observed JWST/NIRSpec data for MoM-BH*-1 at $z = 7.7569$ (black line). The model successfully reproduces the overall continuum shape, the prominent $H\beta$ emission feature, and the adjacent absorption lines. The broad $H\beta$ profile (model FWHM $\approx 3590 \text{ km s}^{-1}$) is achieved by combining intrinsic Stark broadening with a macroturbulent velocity of 1250 km s^{-1} and a stellar wind with a terminal velocity of 1500 km s^{-1} . The underlying continuum from the model is shown as a blue dotted line.

here that our $10^6 M_\odot$ SMS model, when its intrinsic spectrum is processed through a physically motivated broadening pipeline, provides a quantitative match to our two primary targets. The broad, complex line profiles seen in the data are a key diagnostic. Since our underlying stellar model is non-rotating ($v \sin i = 0$), the observed line widths must originate from a combination of physical processes within the star’s photosphere and extended atmosphere.

Our fitting pipeline models the line profiles by convolving the intrinsic spectrum with a series of broadening kernels. The primary mechanisms are: (1) intrinsic Stark broadening, which shapes the far wings of the line profile; (2) a large-scale, isotropic macroturbulent velocity field (σ_v), physically motivated by the same turbulent inflows that are expected to feed the star, which we model as a Gaussian; and (3) a powerful stellar wind (v_∞), modeled as a boxcar. The latter two are the key free parameters used to match the observations.

The High-Redshift Target: MoM-BH-1 ($z = 7.76$).*— Figure 6 presents our best-fit model compared to the JWST/NIRSpec spectrum of MoM-BH*-1. The ob-

served $H\beta$ line in this source is exceptionally broad, with a measured FWHM of 3736 km s^{-1} . Our fitting script systematically varies the macroturbulent velocity to match this width. The best fit, shown as a thin red line, is achieved with a macroturbulent velocity of $\sigma_v = 1250 \text{ km s}^{-1}$ and a wind terminal velocity of $v_\infty = 1500 \text{ km s}^{-1}$. This combination yields a model FWHM of 3590 km s^{-1} , agreeing with the observed value to within 4%. The adopted wind velocity is physically well-motivated; it is a significant fraction ($\sim 40\%$) of the star’s gravitational escape velocity ($v_{\text{esc}} \approx 3800 \text{ km s}^{-1}$), consistent with expectations for a continuum-driven outflow from a luminous supergiant. While 1500 km s^{-1} represents the upper end of our tested range, we find that similar quality fits can be obtained with lower wind velocities, provided the macroturbulence is adjusted to compensate, demonstrating the model’s robustness.

The Lower-Redshift Target: The Cliff ($z = 3.55$).— We apply the same methodology to The Cliff, a similarly luminous LRD at a lower redshift. As shown in Figure 7, our model again provides an excellent match to the observed spectrum. For this target, which has

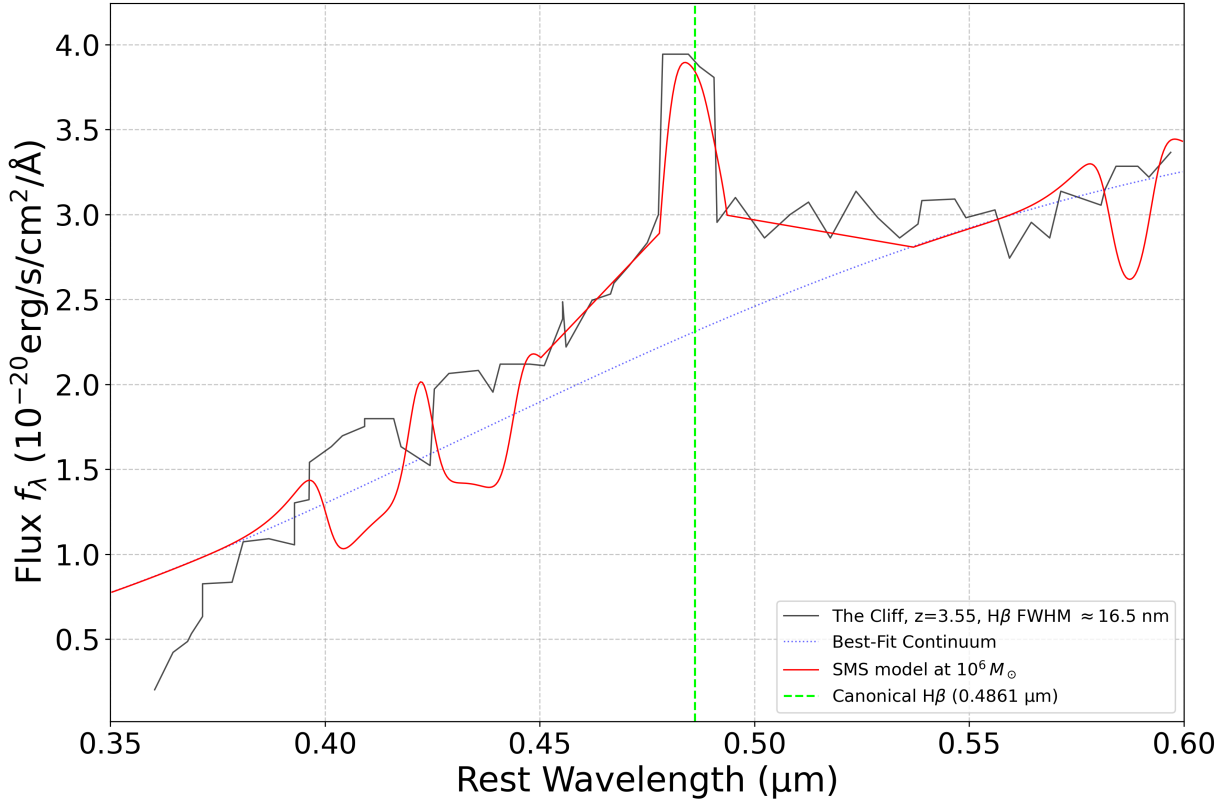


Figure 7. Best-fit synthetic spectrum (thin red line) for our $10^6 M_{\odot}$ SMS model compared to the observed JWST/NIRSpec data for The Cliff at $z = 3.55$ (black line). As with MoM-BH*-1, the model provides an excellent match to the continuum and the broad $H\beta$ and $H\alpha$ emission lines. The fit shown incorporates a macroturbulent velocity of 1500 km s^{-1} , in excellent agreement with the observed $H\alpha$ FWHM, and includes a final smoothing of the line wings via sideband interpolation to precisely match the observed profile shape. The model continuum is shown as a blue dotted line.

a measured broad $H\alpha$ FWHM of $1533_{-80}^{+110} \text{ km s}^{-1}$ (de Graaff et al. 2025), the best fit was achieved with a macroturbulent velocity of $\sigma_v = 1500 \text{ km s}^{-1}$, in direct agreement with the observation. This provides an excellent match to $H\beta$ line eprofile as shown in Figure 7. In this case, to precisely match the shape of the $H\beta$ profile, we also applied a phenomenological correction via sideband interpolation, a feature of our fitting script. This technique, which replaces the flux in the far wings of the line with a linear interpolation, effectively smooths the transition from the line to the continuum and can be seen as an approximation for more complex radiative transfer effects or a more detailed velocity structure not captured in our 1D model.

Despite the simplifications inherent in our modeling, such as the lack of a full comoving-frame radiative transfer solution and the use of phenomenological line boosts, the success of our model is significant. The ability to reproduce the spectra of two distinct LRDs at vastly different cosmic epochs, using a consistent physical framework and justifiable parameters, provides strong evi-

dence that supermassive stars are a compelling explanation for this class of object.

4. SUMMARY AND CONCLUSION

We have presented a first-principles investigation into whether Population III supermassive stars (SMSs) can serve as the central engines for the enigmatic class of objects known as Little Red Dots (LRDs). By developing a novel pipeline that combines a GENEC stellar evolution model with a detailed radiative transfer and spectral synthesis code, we have demonstrated that a single, non-rotating $10^6 M_{\odot}$ SMS can successfully reproduce the key observational features of two prominent LRDs: MoM-BH*-1 at $z = 7.76$ and The Cliff at $z = 3.55$.

Our primary findings are as follows:

- **Luminosity as a Decisive Constraint:** We establish that while SMSs across a range of masses ($\gtrsim 10^5 M_{\odot}$) can produce the requisite spectral shape, only a star with a mass of $10^6 M_{\odot}$ possesses the intrinsic luminosity ($L_{\lambda} \approx 1.7 \times 10^{44} \text{ erg s}^{-1} \mu\text{m}^{-1}$ at 4050 \AA) required to match

the observed brightness of the LRD targets. This immediately sets the necessary mass scale for any viable SMS candidate.

- **A Photospheric Origin for the Balmer Break:** Our model demonstrates that the V-shaped continuum morphology of LRDs is not caused by dust, but is an intrinsic feature of the SMS photosphere. It originates from a powerful Balmer Jump in emission, which itself is driven by a sharp increase in the continuum absorption opacity at 3646 Å from the photoionization of hydrogen from the $n=2$ level.
- **A Unified Mechanism for Line Formation:** We show that the complex Balmer line phenomenology, specifically, the simultaneous presence of $H\beta$ in strong emission and other Balmer lines ($H\gamma$, $H\delta$) in absorption is naturally explained within our single-atmosphere model. This is achieved through differential non-LTE effects, where radiative pumping drives the $H\beta$ source function above the local continuum ($S_L > S_C$), while other lines remain thermalized ($S_L < S_C$).
- **Successful Matching of Observed Spectra:** By applying physically motivated broadening mechanisms, including a powerful stellar wind ($v_\infty \approx 1500 \text{ km s}^{-1}$) and large-scale macroturbulence ($\sigma_v \approx 1250 - 1500 \text{ km s}^{-1}$), our model quantitatively reproduces the broad line profiles observed in both LRD targets, matching the measured FWHM of MoM-BH*-1 to within 4%.

In conclusion, our SMS model provides a remarkably simple and self-consistent physical picture for LRDs. Unlike multi-component AGN models, our framework explains the continuum shape, the line features, and the line widths as emergent properties of a single stellar object. The model provides a unified origin for both the broad emission and the P-Cygni-like absorption features, which are both shaped by the same velocity field originating from the stellar photosphere. This presents a compelling alternative to scenarios that require separate components for emission, absorption, and continuum.

We acknowledge that the short, $\sim 10^3$ yr lifetime of our fiducial SMS model presents a cosmological challenge. If all LRDs correspond to such objects, their observed number density would imply a very large population of remnant $\sim 10^6 M_\odot$ black holes, potentially in tension with constraints from the faint AGN luminosity function. This tension could be alleviated if, for instance, the LRDs we observe represent only the most extreme and rare formation events. Alternatively, physical processes not included in our model, such as stellar rotation, are expected to significantly extend the SMS lifetime, thereby reducing the required birthrate and the number of resulting remnants.

Future work should aim to build upon the foundation laid here. The natural next step is to advance the modeling pipeline by implementing a full, comoving-frame radiative transfer solution to treat the wind and line formation more self-consistently. Expanding the model to include a more detailed multi-level hydrogen atom (i.e., explicitly including the $n=3$ level) is a primary next step, which would allow for a self-consistent prediction of the $H\alpha$ line strength and a more rigorous calculation of the NLTE effects, reducing the reliance on phenomenological boosts. Furthermore, exploring a wider parameter space of SMS models (e.g., varying mass, accretion history, and rotation) could reveal whether a single evolutionary sequence can explain the full diversity of the LRD population. Finally, modeling the expected photometric variability from such dynamically unstable, pulsating objects could provide a powerful, new observational test to distinguish the SMS scenario from its alternatives.

ACKNOWLEDGMENTS

This work was supported in part by the black hole initiative at Harvard University, funded by grants from JTF and GBMF. We thank Andrea Ferrara, Keith Horne, Kohei Inayoshi, and Igor Chilingarian for stimulating discussions and detailed feedback on an earlier version of this manuscript, particularly regarding the presentation of the spectral features, the details of the radiative transfer model, and the broader cosmological implications of our results.

REFERENCES

- Auer, L. H., & Mihalas, D. 1969, *ApJ*, 158, 641, doi: [10.1086/150226](https://doi.org/10.1086/150226)
- Baggen, J. F. W., van Dokkum, P., Brammer, G., et al. 2024, *ApJL*, 977, L13, doi: [10.3847/2041-8213/ad90b8](https://doi.org/10.3847/2041-8213/ad90b8)
- Baumgarte, T. W., & Shapiro, S. L. 1999, *ApJ*, 526, 941, doi: [10.1086/308006](https://doi.org/10.1086/308006)
- Begelman, M. C. 2012, *MNRAS*, 420, 2912, doi: [10.1111/j.1365-2966.2011.20071.x](https://doi.org/10.1111/j.1365-2966.2011.20071.x)

- Bromm, V., & Loeb, A. 2003, *Nature*, 425, 812, doi: [10.1038/nature02071](https://doi.org/10.1038/nature02071)
- de Graaff, A., Rix, H.-W., Naidu, R. P., et al. 2025, arXiv e-prints, arXiv:2503.16600, doi: [10.48550/arXiv.2503.16600](https://doi.org/10.48550/arXiv.2503.16600)
- Fan, X., Strauss, M. A., Becker, R. H., et al. 2006, *AJ*, 132, 117, doi: [10.1086/504836](https://doi.org/10.1086/504836)
- Haemmerlé, L. 2021, *A&A*, 650, A204, doi: [10.1051/0004-6361/202140893](https://doi.org/10.1051/0004-6361/202140893)
- Haemmerlé, L., Woods, T. E., Klessen, R. S., Heger, A., & Whalen, D. J. 2018, *ApJL*, 853, L3, doi: [10.3847/2041-8213/aaa462](https://doi.org/10.3847/2041-8213/aaa462)
- Hosokawa, T., Omukai, K., & Yorke, H. W. 2012, *The Astrophysical Journal*, 756, 93, doi: [10.1088/0004-637x/756/1/93](https://doi.org/10.1088/0004-637x/756/1/93)
- Inayoshi, K., & Maiolino, R. 2025, *ApJL*, 980, L27, doi: [10.3847/2041-8213/adaebd](https://doi.org/10.3847/2041-8213/adaebd)
- Inayoshi, K., Visbal, E., & Haiman, Z. 2020, *ARA&A*, 58, 27, doi: [10.1146/annurev-astro-120419-014455](https://doi.org/10.1146/annurev-astro-120419-014455)
- Killi, M., Watson, D., Brammer, G., et al. 2024, *A&A*, 691, A52, doi: [10.1051/0004-6361/202348857](https://doi.org/10.1051/0004-6361/202348857)
- Kokorev, V., Fujimoto, S., Labbe, I., et al. 2023, *ApJL*, 957, L7, doi: [10.3847/2041-8213/ad037a](https://doi.org/10.3847/2041-8213/ad037a)
- Labbé, I., van Dokkum, P., Nelson, E., et al. 2023, *Nature*, 616, 266, doi: [10.1038/s41586-023-05786-2](https://doi.org/10.1038/s41586-023-05786-2)
- Latif, M. A., Whalen, D. J., Khochfar, S., Herrington, N. P., & Woods, T. E. 2022, *Nature*, 607, 48, doi: [10.1038/s41586-022-04813-y](https://doi.org/10.1038/s41586-022-04813-y)
- Liu, B., Sibony, Y., Meynet, G., & Bromm, V. 2025, *ApJL*, 980, L30, doi: [10.3847/2041-8213/adb151](https://doi.org/10.3847/2041-8213/adb151)
- Loeb, A. 2024, *Research Notes of the American Astronomical Society*, 8, 182, doi: [10.3847/2515-5172/ad614c](https://doi.org/10.3847/2515-5172/ad614c)
- Loeb, A., & Rasio, F. A. 1994, *ApJ*, 432, 52, doi: [10.1086/174548](https://doi.org/10.1086/174548)
- Martins, F., Schaerer, D., Haemmerlé, L., & Charbonnel, C. 2020, *A&A*, 633, A9, doi: [10.1051/0004-6361/20193696310.48550/arXiv.1911.04763](https://doi.org/10.1051/0004-6361/20193696310.48550/arXiv.1911.04763)
- Matthee, J., Naidu, R. P., Brammer, G., et al. 2024, *ApJ*, 963, 129, doi: [10.3847/1538-4357/ad2345](https://doi.org/10.3847/1538-4357/ad2345)
- Mayer, L., Fiacconi, D., Bonoli, S., et al. 2015, *ApJ*, 810, 51, doi: [10.1088/0004-637X/810/1/51](https://doi.org/10.1088/0004-637X/810/1/51)
- Mayer, L., Kazantzidis, S., Escala, A., & Callegari, S. 2010a, *Nature*, 466, 1082, doi: [10.1038/nature09294](https://doi.org/10.1038/nature09294)
- Mayer, L., Kazantzidis, S., Escala, A., & Callegari, S. 2010b, *Nature*, 466, 1082, doi: [10.1038/nature09294](https://doi.org/10.1038/nature09294)
- Naidu, R. P., Matthee, J., Katz, H., et al. 2025, arXiv e-prints, arXiv:2503.16596, doi: [10.48550/arXiv.2503.16596](https://doi.org/10.48550/arXiv.2503.16596)
- Nandal, D., Buldgen, G., Whalen, D. J., et al. 2025a, arXiv e-prints, arXiv:2506.08268, doi: [10.48550/arXiv.2506.08268](https://doi.org/10.48550/arXiv.2506.08268)
- Nandal, D., Farrell, E., Buldgen, G., Meynet, G., & Ekström, S. 2024a, *A&A*, 685, A159, doi: [10.1051/0004-6361/202345997](https://doi.org/10.1051/0004-6361/202345997)
- Nandal, D., Regan, J. A., Woods, T. E., et al. 2023, *A&A*, 677, A155, doi: [10.1051/0004-6361/202346938](https://doi.org/10.1051/0004-6361/202346938)
- Nandal, D., Whalen, D. J., Latif, M. A., & Heger, A. 2025b, arXiv e-prints, arXiv:2502.04435, doi: [10.48550/arXiv.2502.04435](https://doi.org/10.48550/arXiv.2502.04435)
- Nandal, D., Zwick, L., Whalen, D. J., et al. 2024b, *A&A*, 689, A351, doi: [10.1051/0004-6361/202449562](https://doi.org/10.1051/0004-6361/202449562)
- Natarajan, P. 2021, *MNRAS*, 501, 1413, doi: [10.1093/mnras/staa3724](https://doi.org/10.1093/mnras/staa3724)
- Pacucci, F., & Loeb, A. 2022, *MNRAS*, 509, 1885, doi: [10.1093/mnras/stab3071](https://doi.org/10.1093/mnras/stab3071)
- Pacucci, F., & Loeb, A. 2025, arXiv e-prints, arXiv:2506.03244, doi: [10.48550/arXiv.2506.03244](https://doi.org/10.48550/arXiv.2506.03244)
- Schleicher, D. R. G., Fellhauer, M., Boekholt, T. C. N., et al. 2019, *Boletín de la Asociación Argentina de Astronomía La Plata Argentina*, 61, 234, doi: [10.48550/arXiv.1812.02052](https://doi.org/10.48550/arXiv.1812.02052)
- Übler, H., Maiolino, R., Pérez-González, P. G., et al. 2024, *MNRAS*, 531, 355, doi: [10.1093/mnras/stae943](https://doi.org/10.1093/mnras/stae943)
- Volonteri, M., Habouzit, M., & Colpi, M. 2021, *Nature Reviews Physics*, 3, 732, doi: [10.1038/s42254-021-00364-9](https://doi.org/10.1038/s42254-021-00364-9)
- Woods, T. E., Heger, A., Whalen, D. J., Haemmerlé, L., & Klessen, R. S. 2017, *ApJL*, 842, L6, doi: [10.3847/2041-8213/aa7412](https://doi.org/10.3847/2041-8213/aa7412)
- Zhang, Z., Jiang, L., Liu, W., & Ho, L. C. 2025, *ApJ*, 985, 119, doi: [10.3847/1538-4357/adcb3e](https://doi.org/10.3847/1538-4357/adcb3e)
- Zwick, L., Mayer, L., Haemmerlé, L., & Klessen, R. S. 2023, *MNRAS*, 518, 2076, doi: [10.1093/mnras/stac3204](https://doi.org/10.1093/mnras/stac3204)